This article has been accepted for publication in a future issue of this journal, but has not been fully edited. Content may change prior to final publication. Citation information: DOI 10.1109/TBCAS.2019.2953579, IEEE Transactions on Biomedical Circuits and Systems

An Integrated Biosensor System with a High-Density Microelectrode Array for Real-Time Electrochemical Imaging

William Tedjo, *Student Member, IEEE*, Thomas Chen, Senior *Member, IEEE*

Abstract—Electrochemical methods have been shown to be advantageous to life sciences by supporting studies and discoveries in metabolism activities, DNA analysis, and neurotransmitter signaling. Meanwhile, the integration of Microelectrode Array (MEA) and the accessibility of CMOS technology permit high-density electrochemical sensing method. This paper describes an electrochemical imaging system equipped with a custom CMOS microchip. The microchip holds a 3.6mm×3.6mm sensing area containing 16,064 Pt MEA, the associated 16,064 integrated read channels, and digital control circuits. The novel three-electrode system geometry with a 27.5µm spatial pitch enables cellular level chemical gradient imaging of bio-samples. The noise level of the on-chip read channel array allows amperometric detection of neurotransmitters such as norepinephrine (NE) with concentrations from 4µM to 512µM with 4.7pA/µM sensitivity (R^2=0.98). Electrochemical response to dissolved oxygen (DO) concentration was also characterized by deoxygenated deionized water containing 5% to 80% of the ambient oxygen concentrations with 86pA/mg/L sensitivity (R^2=0.89). The system also demonstrated selectivity to different target analytes using cyclic voltammetry method to simultaneously detect NE and uric acid. Also, a custom indium tin oxide with deposited Au glass electrode was integrated into the microfluidic system to enable pH measurement, ensuring the viability of bio-samples during experiments. Electrochemical images confirm the spatiotemporal performance at four frames per second while maintaining the sensitivity to target analytes. Finally, the overall system is controlled and continuously monitored by a MATLAB-based custom user interface, which is optimized for real-time high spatiotemporal resolution chemical imaging.

Index Terms—Microelectrode array, CMOS circuit design, biosensor system integration, instrumentation, electrochemistry, analytical chemistry, amperometry, voltammetry, microfluidic.

I. Introduction

ELECTROCHEMICAL sensing for detecting specific analytes has allowed integration with other ex vivo or in vitro bioanalytical platforms (e.g. microfluidics systems and other microscopy techniques). The electrochemical methods support and enable biological discoveries that were difficult to achieve in the past. Recent applications of electrochemical sensing include studies in: metabolism activities by sensing levels of dissolved oxygen (DO)[1]–[3], glucose, lactate, and pyruvate [4]–[6]; roles of nitric oxide in physiology [7], [8]; DNA hybridization and analysis [9], [10]; and understanding complex roles of neurotransmitters in cell growth, communications, and deaths [11], [12]. Furthermore, applications of Microelectrode Arrays (MEAs) in electrochemical sensing have provided significantly enhanced spatial resolution for enabling studies of cell-to-cell signaling pathways and other complex biological phenomena. Sensor devices employing MEAs were first reported by Thomas [13] and further improved by others [14]–[16] to illustrate their capabilities of recording two-dimensional action potentials to better understand the biological signaling mechanism. The manufacturing compatibility of MEAs with CMOS technology allows tight integration of MEAs and supporting sensor circuitry within a single silicon substrate. Such compatibility provides the necessary performance needed to achieve high temporal resolution. Simultaneously, accessibility to CMOS processes offers a low-cost solution for integrating customized and complex electronic circuits with a higher signal-to-noise ratio (SNR). A biosensor system that combines electrochemical methods and CMOS technologies would benefit the life-science community by providing real-time chemical images at high spatial and temporal resolutions.

The integration of MEA fabrication and CMOS technology into biosensing applications requires integration of multi-disciplinary knowledge in electronics circuit design, analytical chemistry, and physiology. Currently, there is a spectrum of MEA biosensors with CMOS technology that focuses on electrophysiology, impedancemetry, and electrochemistry. Electrophysiology-focused MEA systems emphasize studies on action potential signal acquisition and stimulation of neuronal cells up to hundreds of hertz [17]–[20]. The addition of impedance measurements in an MEA configuration assists the determination of biological conditions of target cells or tissue samples [21]. Multimodal MEA systems integrate multiple biosensing functionalities, such as optical and temperature sensing, in addition to electrophysiology and impedance measurements [22], [23]. The existing electrochemical MEA systems emphasize on sensing electrochemically active substances with integrated CMOS technology [24]–[34] and without integrated CMOS technology [35]–[37]. The existing designs of MEA-based systems provide valuable insights into two-dimensional electrochemical sensing. However, the existing systems present limitations in chemical imaging for bio-samples due to limited spatial resolution for cellular-level imaging, insufficient temporal resolutions to capture the chemical gradient actions over time, or low SNR read channels for micromolar concentration sensing.

The biosensor system presented in this paper focuses on the common electrochemical sensing modalities (voltammetry and amperometry) and all-around advancements to the existing

This work was partially supported by two grants from the National Science Foundation (GDE-0841259 and GDE-1450032). *(Corresponding author: Thomas Chen.)*

W. Tedjo and T. Chen are with Department of Electrical & Computer Engineering and School of Biomedical Engineering, Colorado State University, Fort Collins, CO 80523, USA. (e-mail: Thomas.Chen@colostate.edu).

1932-4545 (c) 2019 IEEE. Personal use is permitted, but republication/redistribution requires IEEE permission. See http://www.ieee.org/publications_standards/publications/rights/index.html for more information.

This article has been accepted for publication in a future issue of this journal, but has not been fully edited. Content may change prior to final publication. Citation information: DOI 10.1109/TBCAS.2019.2953579, IEEE Transactions on Biomedical Circuits and Systems

MEA-based electrochemical sensing systems. Various design aspects of the MEA biosensor system presented in this paper are based on our established work with electrode geometry to maximize electron transfer efficiency by increasing electrode perimeter and area [38]. The system utilizes the electrochemical reduction-oxidation (redox) mechanism with a three-electrode configuration consisting of Working Electrode (WE), Reference Electrode (RE), and Auxiliary Electrode (AE). An earlier version of the biosensor CMOS MEA microchip was tested with microfluidic flow injection experiments to demonstrate its chemical imaging capability [39], [40]. Incorporating the same CMOS MEA microchip, an improved system with significantly higher SNR verified the viability of high resolution spatiotemporal electrochemical imaging in stimulated tissue ex vivo experiments [29], [41]. The chemical images from the prior system demonstrated its potential as a tool for studying real-time cell-cell signaling of live tissues. However, the performance of the previous generations of our CMOS MEA microchip suffered from three major limitations. First, the extended signal settling time is required during the multiplexing process of connecting read channels to the WE array in the MEA. The multiplexing process, though only a few seconds long, disturbs the continuity of the electrochemical cell and lowers the temporal resolution. Second, each WE accumulate random current leakage up to 100nA due to direct connections to an array of analog CMOS switches (transmission gates) as part of the multiplexing scheme. This leakage current heavily impacts the read channel's overall SNR performance because the electrochemical signal is observed to be within pA to few nA from a single WE. Third, the arrangement of the three-electrode system is not optimal for dense MEA configuration. The sparsely placed RE and AE blocks impose irregular readings across the WE array, creating the proximity effect of high reading values closer to AE blocks within a sub-array. This artifact is shown as repeating stripes or block patterns in the previously published chemical image results [29], [39]. Also, unbounded and tightly packed WEs generate heavily overlapping diffusion layer, which is not desirable when obtaining high signal-to-background current ratio in scanning voltammetry methods [42], [43].

This paper describes a fully customized design of an electrochemical biosensor system. The presented system employs a custom CMOS microchip with 16,064 Pt MEA at 27.5µm pitch and a compact system to support chemical imaging of live biological samples with up to four frames per second (FPS). The new system design addresses issues from the previous generation [29] at the CMOS microchip level while maximizing the integration of other features at the board level, which includes device monitoring (e.g. power consumption and temperature sensing points), control circuits for MEA multiplexing, and microfluidic system with pH monitoring. In comparison with previous design [29], [41], the new design increases the number of WEs and area coverage from 8,192 (2.0mm×2.0mm) to 16,064 (3.6mm×3.6mm), and its uniform geometrical arrangement of the three-electrode system helps to minimize the diffusion layer overlaps. Arrays of compact on-chip current to voltage (I-V) amplifier circuits (read channels) are individually connected to each corresponding WE without intermediate multiplexing analog switches or current buffers. The only on-chip multiplexing occurs at the voltage outputs of the read channels. This configuration was selected to ensure the continuation of electrochemical cell redox reaction and to minimize any disturbance to the noise-sensitive electrochemically active samples at the WE surface. Therefore, the new design allows faster data acquisition scheme to scan through all 16,064 read channels. Significant temporal improvement was achieved with the generation of a 16-thousand pixel chemical image in every 0.25 seconds, while the previous generation required at least 30 seconds to generate an 8,192-pixel single-frame chemical image. At the board level, the control and support circuits were designed around a microcontroller unit (MCU). The entire system is controlled and monitored in real-time using a custom-built Graphical User Interface (GUI) on a host computer. Microfluidic flow injection experiments of neurotransmitter (norepinephrine (NE)) and deoxygenated deionized water (DI-H_2O) confirmed the sensitivity performance and high spatiotemporal fidelity. The cyclic voltammetry (CV) results showed feasibility in simultaneous detections of different target analytes in all 16,064 WEs. This system not only presents significantly improved performance from the exiting works but also provides an all-in-one high spatiotemporal chemical biosensing system solution for practical applications.

The remaining part of the paper is organized as follow: Section II provides a brief overview of the biosensor system. Section III presents the details of the integrated circuit design and the MEA layout of the custom CMOS MEA microchip. Section IV describes the board-level integration. System-level integration of microfluidic, data processing, and user interfaces are presented in Section V. Section VI describes the experimental setup and the chemicals and materials used in the experiments. Measurement results, both quantitatively (calibration curves) and qualitatively (two-dimensional heatmaps), are shown in Section VII. Finally, discussions and conclusions are given in Section VIII.

II. Biosensor System Overview

The electrochemical biosensor system, as illustrated in Fig. 1, comprises of the custom CMOS MEA microchip, three custom Printed Circuit Boards (PCBs), a Power Supply Unit (PSU), a commercial Data Acquisition (DAQ), and a host computer running the GUI. The Sensor PCB (S-PCB) holds the CMOS MEA microchip socket and voltage linear regulators to supply controllable low-noise power to the CMOS MEA microchip and the C-PCB. A custom Control PCB (C-PCB) consists of a Microcontroller Unit (MCU), analog and digital signal generators, voltage monitoring circuits, and a USB interface for communication with the host computer. A Shield PCB (Sh-PCB) with a custom heatsink provides excess thermal removal for the CMOS MEA microchip and protects analog signals in S-PCB from electromagnetic interference (EMI) from digital control signals on C-PCB. A DAQ board, ADLINK DAQ-2208 (ADLINK, New Taipei, Taiwan), converts analog voltage readings from the CMOS MEA microchip to 12-bit digital signals to be processed and stored in the host computer. The control and display software and its GUI on the host computer is written in MATLAB. The GUI reports processed biosensing results, shows the information gathered from the C-PCB, and allow users to perform real-time system control.

1932-4545 (c) 2019 IEEE. Personal use is permitted, but republication/redistribution requires IEEE permission. See http://www.ieee.org/publications_standards/publications/rights/index.html for more information.

This article has been accepted for publication in a future issue of this journal, but has not been fully edited. Content may change prior to final publication. Citation information: DOI 10.1109/TBCAS.2019.2953579, IEEE Transactions on Biomedical Circuits and Systems

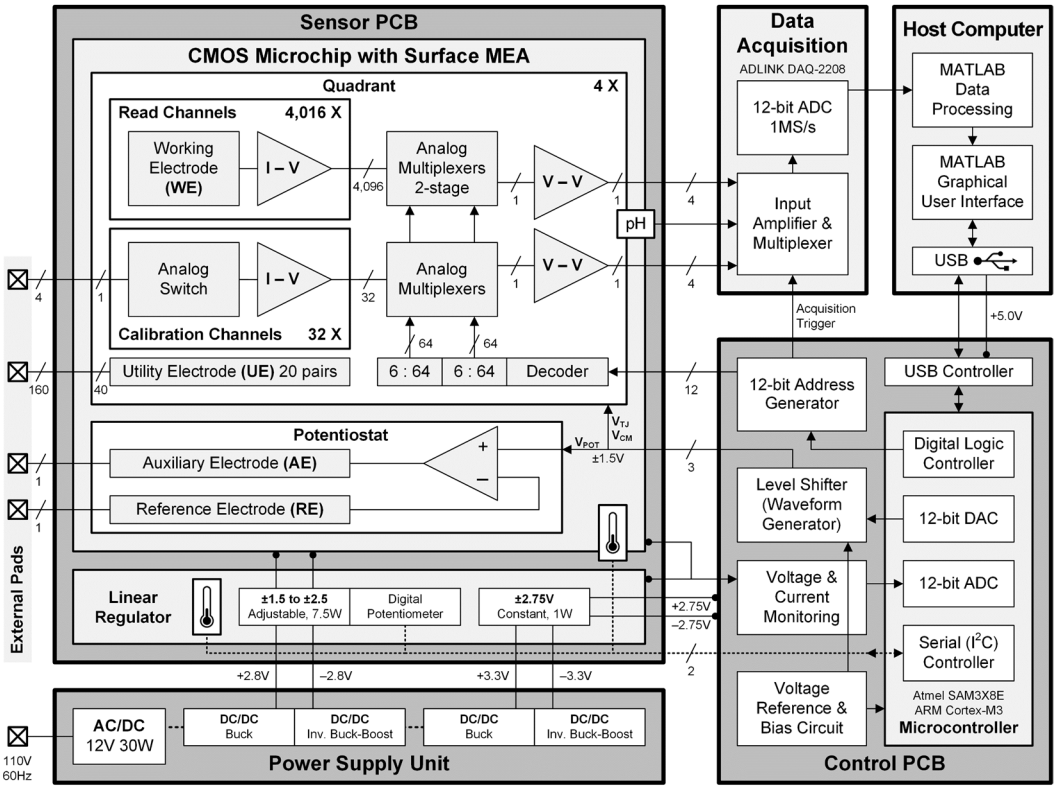

Fig. 1. Electrochemical biosensor system functional block diagram.

III. CMOS MEA Microchip

The CMOS MEA microchip holds the surface MEA and the read channel array, where the electrochemical electron transfer and current to voltage (I-V) conversion occur, respectively. The on-chip read channel outputs are multiplexed and buffered to the external I/O pads. To assist the three-electrode electrochemical analysis, an on-chip potentiostat is employed.

The CMOS MEA microchip was custom designed on a standard 0.6µm and 3-metal layer CMOS process with an additional metal layer as the surface MEA. As shown in Fig. 2, the 19mm×19mm silicon die was placed and wire bonded to a cavity-up ceramic 280-pin pin-grid-array (PGA) package. The choice of the 0.6µm CMOS process is mainly due to the availability of its post-platinization process for the MEA. The 0.6µm CMOS process allows the 27.5µm spatial resolution, a size within the range of the typical cell pitch (30µm to 50µm) in live bio-sample tissue. Therefore, it allows spatial differentiation of the chemical activities at the cellular level. The post-platinization process for the MEA was described in [29], [38]. The fabrication of CMOS MEA microchip and its surface MEA was provided by Broadcom Inc. (San Jose, CA, United States).

At its surface, the CMOS MEA microchip holds 128×128 or 16,064 WEs, 80 pairs of general-purpose interdigitated Utility Electrodes (UEs), and one shared interleaved RE and AE. Each pair of UE takes an area of four WEs, hence, there are 16,064 total WEs instead of 16,384. The MEA covers an area of 3.6mm×3.6mm. The array of WEs and read channels are compartmentalized into quadrants and group of columns with all 16,064 WEs individually connected to 16,064 on-chip read channels. Electrode selection can be customized to form a desirable two-dimensional pattern through the analog multiplexers and digital control logic. As depicted in Fig. 2, the quadrants are mirrored, vertically and horizontally, for the benefit of matching and modularity of floorplan layout. In an outwards order: MEA, metal routing bus, read channel array, two-stage multiplexing, and control logic are in the direction towards each quadrant corner. This specific floorplan was chosen to maximize the MEA density at the center and distribute the read channel outward, accommodating chemical imaging of up to 3.6mm×3.6mm size live tissues with cellular-level resolution. This similar topology was used in high-density MEA integration [21], [24], [27], [29], while the in-pixel circuits topology limits the MEA density [26], [31], [32], [34].

The CMOS MEA microchip contains a total of 1.2 million CMOS transistors, optimized to operate within ±1.5V and ±2.5V supply rails. The choice for power supply voltage is determined by the microchip's surface MEA temperature and the upper limit of the read channel dynamic range (the expected maximum input current (I_{IN})). For most biosensing application, the desirable surface MEA temperature is 37±0.5°C, which corresponds to a voltage supply of around ±1.65V, depending on the ambient temperature. To increase system flexibility for different chemical imaging applications, the overall power dissipation can be reduced by power gating the read channels in each independently selected quadrant. Power dissipation of the entire CMOS MEA microchip is measured at 957mW (59.6µW/channel) for ±1.65V with all four quadrants turned on, and as low as 159mW (39.6µW/channel) for ±1.5V with only one quadrant turned on.

A. On-chip Read Channel Circuit

Input current to output voltage conversion is performed by a continuous Trans-Impedance Amplifier (TIA). The opamp

1932-4545 (c) 2019 IEEE. Personal use is permitted, but republication/redistribution requires IEEE permission. See http://www.ieee.org/publications_standards/publications/rights/index.html for more information.

This article has been accepted for publication in a future issue of this journal, but has not been fully edited. Content may change prior to final publication. Citation information: DOI 10.1109/TBCAS.2019.2953579, IEEE Transactions on Biomedical Circuits and Systems

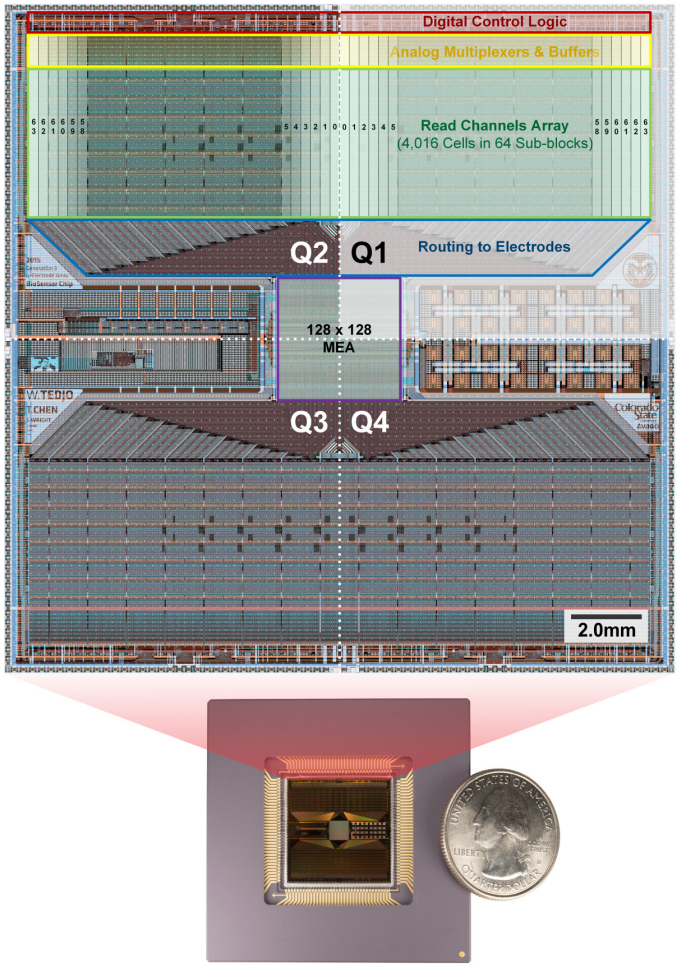

Fig. 2. A micrograph of the CMOS MEA microchip layout with four identical quadrants and classifications of the circuit functions based on location in the microchip. In a quadrant, the read channel array is further arranged to 64 vertical columns, each containing 64 read channel cells.

topology is based on a folded cascode structure with complementary NMOS-PMOS input stage and a push-pull output stage (see Section 1 of Supplementary Materials). This configuration was chosen to maximize input and output rail-to-rail swing. A T-network feedback resistor configuration was selected to accommodate the area constraints involved in fitting 16,064 read channels and the large transimpedance gain.

As depicted in Fig. 3, the OP_{TIA} with $R_{1\text{-}3}$ forms the T-network TIA. OP_{TJ} in unity-gain configuration provides voltage buffering and isolation from an off-chip external bias source (V_{TJ}). The double-layer capacitance formation at WE surface is approximated as C_{DL}, while the interconnect routing parasitic from WE to TIA input is modeled as R_{RT} and C_{RT}. C_{RT} was extracted to be ~1pF and C_{DL} was approximated to be 100pF. The C_{DL} approximation uses the worst-case scenario capacitance coefficient (250μF/cm^2) based on a previous study [44] and the WE surface area (427.5μm^2). Therefore, the capacitance at the TIA input node is expected to be dominated by C_{DL}. A feedback capacitor (C_F) limits the TIA and its noise bandwidth and provides compensation to ensure transient response stability. The equivalent resistance is defined by Eq. (1), resulting in output potential shown in Eq. (2). Assuming constant 0V and low-noise voltage sources are connected to V_{CM} and V_{TJ}, the I-V conversion is simplified to Eq. (3).

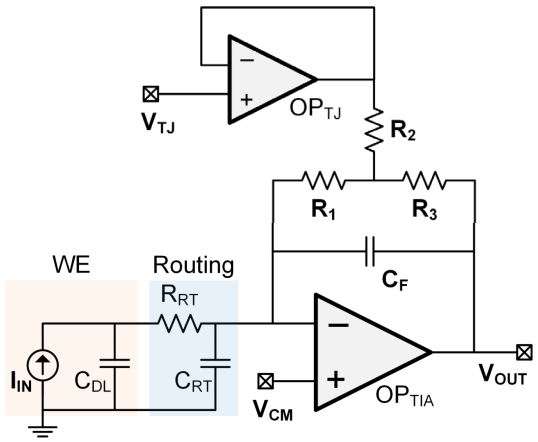

Fig. 3. The trans-impedance amplifier read channel with high gain T-network resistive feedback for silicon area optimization.

$$R_{EQ} = R_1 + R_3 + \left(\frac{R_1 \cdot R_3}{R_2}\right) \approx R1 \cdot \left(1 + \frac{R_3}{R_2}\right) \quad (1)$$

$$V_{OUT} = -I_{IN} \cdot R_{EQ} + \left(1 + \frac{R_3}{R_2}\right) \cdot V_{CM} - \left(\frac{R_3}{R_2}\right) V_{TJ} \quad (2)$$

$$V_{OUT} = -I_{IN} \cdot R_1 \cdot \left(1 + \frac{R_3}{R_2}\right) \quad (3)$$

The Common Mode Voltage (V_{CM}) and T-Network Feedback Voltage (V_{TJ}) are globally shared and their voltage potentials can be customized off-chip. V_{CM} defines the potential of WEs and should be set at constant 0V for electrochemical reading, or pulsed for electrode cleaning [40], [45]. V_{TJ} should be finely adjusted to regulate the V_{OUT} DC offset near 0V, the middle voltage potential between the power supply rails.

The T-network noise performance is defined by the product of noise sources (i.e. resistor thermal noise and opamp noise) and the inversed feedback factor or noise gain (1/β). Equations (4) and (5) describe the noise gain of a traditional single resistor (R_F) TIA and a T-network TIA, respectively. Fig. 4(a) illustrates the OP_{TIA} open-loop gain associated with the noise gain for both TIA cases with equal resistive feedback values ($R_F = R_{EQ}$). At DC, the T-network configuration demonstrates noise gain magnitude of ($1+ R_3/R_2$) in comparison to the unity-gain in the single resistor TIA, showing that the T-network configuration amplifies the low-frequency noise of OP_{TJ} and OP_{TIA} by ($1+ R_3/R_2$). While keeping the same R_{EQ}, reducing ($1+ R_3/R_2$) and increasing R_1 would push the T-network zero (f_{zT}) approaching the single resistor zero (f_z) at a lower frequency.

$$\frac{1}{\beta(s)} = \frac{f_z(s)}{f_{pf}(s)} = \frac{1+R_F(C_{DL}+C_F)(s)}{1+R_F C_F(s)} \quad (4)$$

$$\frac{1}{\beta_T(s)} = \frac{f_{zT}(s)}{f_{pf}(s)} = \left(1 + \frac{R_3}{R_2}\right)\left(\frac{1+R_1(C_{DL}+C_F)(s)}{1+RC_F(s)}\right) \quad (5)$$

$$V_n = \left(1 + \frac{R_3}{R_2}\right)\sqrt{\left(e_{nR_1}{}^2 + e_{ne}{}^2 + e_{nTJ}{}^2 + e_{ni}{}^2\right)} \quad (6)$$

The total rms output noise (V_n) in a T-network TIA can be summarized to Eq. (6), where e_{nR_1} is the thermal noise of R_1, e_{ne} and e_{nTJ} are the opamp noise of OP_{TJ} and OP_{TIA}, respectively, and e_{ni} is the noise generated by the opamp input bias current, a negligible value in the CMOS process. All noise components are amplified by ($1+R_3/R_2$). Considering the area and power dissipation constraints and noise gain behavior of

1932-4545 (c) 2019 IEEE. Personal use is permitted, but republication/redistribution requires IEEE permission. See http://www.ieee.org/publications_standards/publications/rights/index.html for more information.

This article has been accepted for publication in a future issue of this journal, but has not been fully edited. Content may change prior to final publication. Citation information: DOI 10.1109/TBCAS.2019.2953579, IEEE Transactions on Biomedical Circuits and Systems

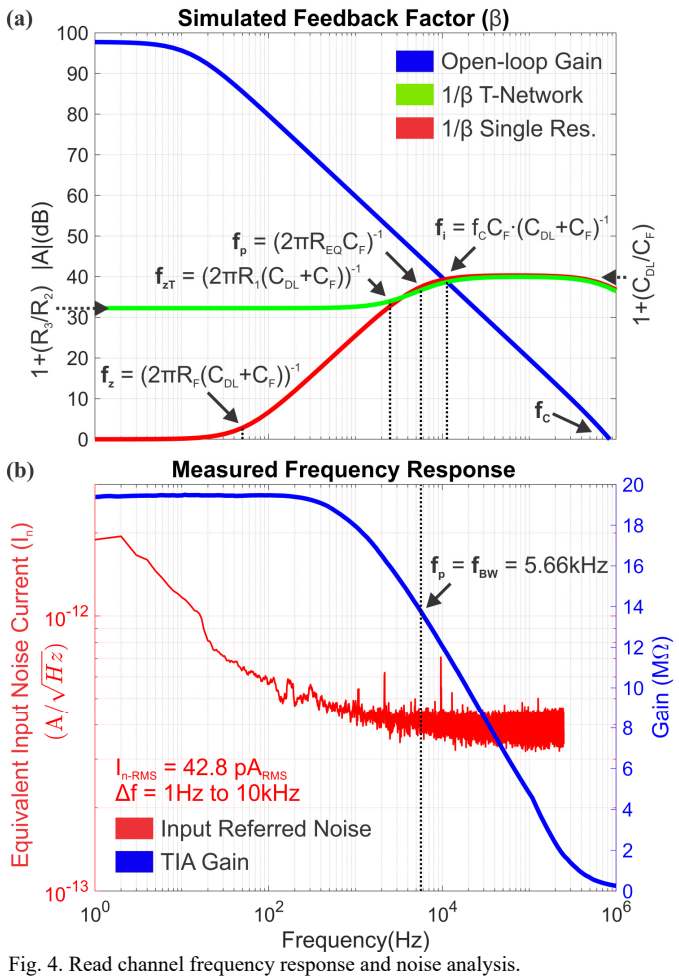

Fig. 4. Read channel frequency response and noise analysis.

TIA using T-network, the 1/f noise of OP_{TIA} and OP_{TJ} are expected to dominate V_n. Therefore, minimizing 1/f noise of the opamp input stage and careful balancing between R_1 and R_3/R_2 were the highest priority for optimizing the noise performance of the read channel.

Stability performance of a TIA is defined at higher frequency, specifically, at the intersection between the noise gain and the OP_{TIA} open-loop gain at f_i. A stable TIA requires $f_p \leq f_i$, when the noise gain is at 0db/decade rate when intersecting the -20dB/decade open-loop gain. The 20db/decade difference at the intersect point indicates a 45º TIA phase margin. An illustration in Fig. 4(a) shows that larger C_{DL} pushes f_{zT} and f_i to a lower frequency and raises the $(1+C_{DL}/C_F)$ plateau while leaving f_p unchanged. An extremely large C_{DL} could push f_i lower than f_p, causing noise gain to intersect the OP_{TIA} open-loop gain at +20db/decade, generating unstable condition. Therefore, a proper approximation of C_{DL} is needed to optimize the TIA stability while minimizing C_F.

Based on previous results of electrochemical ex vivo experiments [29], the equivalent feedback resistance (R_{EQ}) of the TIA is set to $R_{EQ} = 20M\Omega$ ($R_1 = 480k\Omega$, $R_2 = 0.6k\Omega$, and $R_3 = 24k\Omega$). $R_{1\text{-}3}$ values were selected to accommodate the upper limits of the input current dynamic range to tens of nanoamperes without sacrificing sensitivity due to the noise gain factor ($1+ R_3/R_2$). C_F is set at 1pF to maintain stable transient response with the worst-case approximated C_{DL} value of 100pF. Fig. 4(b) shows the TIA gain, bandwidth, and integrated noise responses measurement of 19.6MΩ, 5.66kHz, and 42.8pA_{RMS}, respectively. The bandwidth of the read channel is suitable to capture the chemical molecule diffusivity action in fluid, approximated between 0.1 to 10µm²/ms, within the 27.5µm spatial resolution. The integrated noise frequency range of 1Hz to 10kHz was defined to incorporate low frequency noise close to DC and approximately up to twice of the TIA bandwidth. Table I summarizes the measured TIA read channel specifications and the opamp extracted layout simulation results with additional parallel output RC loads to model the TIA resistive feedback and the parasitic capacitance of the interconnects.

TABLE I
OPAMP AND TIA SPECIFICATIONS

Opamp – Extracted & Simulated				TIA – Measured			
Parameter	Condition	Val.	Unit	Parameter	Condition	Val.	Unit
Ao	DC	97.7	dB	Gain		19.6	MΩ
Offset	G = 1	3.34	mV-σ		variation	0.48	MΩ-σ
PM		51.9	°	Offset	I_{IN} = 0A	5.81	nA-σ
BW	-3dB	12.6	Hz	BW	-3dB	5.66	kHz
GBWP		844	kHz				
Input Noise	1Hz	1.66	µV/√Hz	Input Noise	1Hz	1.89	pA/√Hz
	100Hz	0.29	µV/√Hz		100Hz	0.57	pA/√Hz
	10kHz	0.06	µV/√Hz		10kHz	0.44	pA/√Hz
	1Hz-10kHz	10.4	μV_{RMS}		1Hz-10kHz	42.8	pA_{RMS}
Output Range	to V_{DD}+	0.32	V	Output Range	Max	72.3	nA
	to V_{DD}–	0.34	V		Min	-74	nA
Power	G = 1	55	µW	Power	I_{IN} = 0A	59.6	µW
Dimension	33.05 × 130.40		µm	Area	33.05 × 257.85		µm

* Opamp simulation: $V_{DD} = \pm 1.65V$, T = 37.0ºC, $R_L = 25k\Omega$, $C_L = 2pF$.
* TIA Measurement: $V_{DD} = \pm 1.65V$, T = 37.0ºC, $C_{DL} = 100pF$, $C_L = 2pF$.

B. *On-chip Potentiostat Circuit*

The on-chip potentiostat circuit utilizes a single-opamp configuration with the same topology as the opamp of the TIA, however, with higher output driving strength. In the CV mode, the output stage was designed to handle up to 5kV/s scan rate while driving millifarads capacitive load at the AE, the worst-case estimation of C_{DL} forms at the surface of AE and RE. For an additional flexibility, the on-chip potentiostat can be fully disabled to allow an external on-board potentiostat to takeover and connect to the on-chip AE and RE.

C. *Surface Electrode Layout*

As shown and compared in Fig. 4(a), the improved surface MEA configuration used the same fabrication process based on our previous designs [29], [38]. Each pair of C-shaped electrodes are shorted at the lower metal layer to form a single WE to cover a 17.5µm×17.5µm cross-section area. The WE array is configured in a uniform horizontal and vertical pitch of 27.5/27.5µm. Incorporating the 1.5µm electrode height, a WE surface area is improved by 37% from 317.5µm² to 427.5µm² in comparison the previous WE geometry in [29], which is the main factor in determining the amount of steady-state current density in microelectrode [46].

The improved RE and AE are 2.5µm wide metal line which encloses and interleaves within the WE array. The interleaved RE and AE geometry create an enclosed area around each WE to reduce the effect of overlapping diffusion area within WE and to improve the localization of redox cycle in the highly

1932-4545 (c) 2019 IEEE. Personal use is permitted, but republication/redistribution requires IEEE permission. See http://www.ieee.org/publications_standards/publications/rights/index.html for more information.

This article has been accepted for publication in a future issue of this journal, but has not been fully edited. Content may change prior to final publication. Citation information: DOI 10.1109/TBCAS.2019.2953579, IEEE Transactions on Biomedical Circuits and Systems

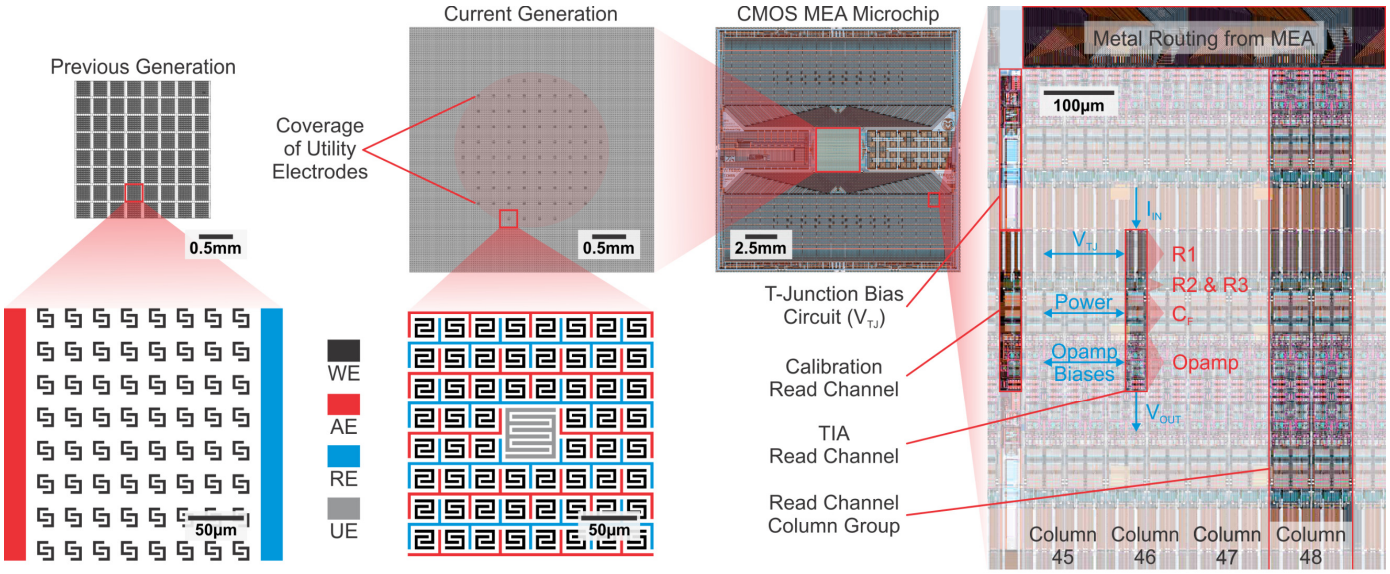

(a) Electrode Array Layout: an 8 × 8 segment comparison with the UE

(b) Read Channel Array Layout

Fig. 5. (a) A segment of MEA showing 8×8 WE array comparing the geometrical modification over previous generation microchip's MEA configuration. The current generation configuration shows a more compact WE array with alternating AE and RE in comparison with the previous generation electrode configuration with two large blocks of AE and RE confining a sparse array of WEs. One pair of UE, a four-finger interdigitated electrode, with four times the size of WE, is also shown in this segment of the current generation of MEA. There are 80 UEs pair evenly distributed in the center area of the MEA. (b) Read channel array configuration with highlighted sections illustrating a single read channel, read channel group columns, a calibration channel, a bias circuit, and metal routings.

dense WE array [27], [31], [47]. The RE and AE are shared among all WEs and can be connected to the on-chip or external potentiostat. In addition, there are 80 pairs of interdigitated UEs distributed around the center area of the MEA array. With a minor spatial compromise of four WEs per UE, each UE provides direct access from the surface MEA to the external I/O pads to allow future integration of biosensing features, such as impedance sensing and electrical stimulation.

D. Read Channel Array Layout

Fig. 5(b) depicts the silicon layout of the read channel array. As reflected by the read channel schematic in Fig. 3, R_1 (480kΩ) uses a high sheet resistivity but a low-precision N-type material, whereas R_2 (0.6kΩ) and R_3 (24kΩ) use a high-precision but low sheet resistivity polysilicon material. This arrangement creates approximately 20MΩ equivalent feedback resistance with 15× smaller layout footprint than an equivalent 20MΩ low-precision N-type resistor. R_3 and R_2 were matched to minimize the R_3/R_2 variation across the read channel array. Due to the noise amplification by the T-network configuration, careful placement and layout around the junction were carried out to minimize crosstalk. The middle connection between $R_{1\text{-}3}$ was kept short to reduce parasitic capacitance down to extracted value of 7.5fF. Also, the buffered V_{TJ} connection was routed through shielded interconnect to R_2 in each read channel with maximum parasitic resistance and capacitance extracted values of 0.4Ω and 0.55pF, respectively. The V_{TJ} voltage biasing is handled by the unity-gain voltage buffers (OP_{TJ}), where each buffer drives 64 read channels in its proximity. In addition, calibration read channels with external input and output access are evenly distributed in the read channel array to verify the I-V functions and to measure the circuits array variations. There are 32 calibration read channels per quadrant multiplexed to a pair of input and output pins.

Each read channel circuit is closely associated with neighboring read channels with shared silicon substrate and metal routing patterns vertically and horizontally. The input current and output voltages were routed vertically (metal 3 layer), whereas voltage biases (e.g. V_{CM} and V_{TJ}) and power lines are shared horizontally (metal 2 layer). This metal routing pattern was used to accommodate modularity between read channels and the limitations of the three metal layers available in this CMOS process.

E. Hierarchical Read Channel Circuit and Control Logic

In each quadrant, an array of 4,016 read channels is divided into 64 column groups. This column grouping can be visualized as thin columns shown in Fig. 2 and Fig. 5(b) and is considered as the first stage of the multiplexing structure to get the WE current signals out to the pins. As shown in Fig. 6, each multiplexer contains 64 analog transmission gates (TG) with ~1.0kΩ on-resistance. The TGs are controlled by a 64-wide logic bus driven by a 6-to-64 logic decoder. The second stage multiplexing structure uses the identical multiplexers to further reduce the selection from 64 column groups to one output. At any given time, only one from 4,016 read channels in each quadrant is selected and its output voltage is buffered to the output pin assigned to the corresponding quadrant, labeled as V_{OUT}Qx, where x = 1,2,3,4. This configuration allows the selected signal from the TIA at the first stage to propagate to the quadrant output within 1µs, allowing scanning time of all 4,016 read channels of a quadrant in 4.1ms. A custom address cycles can be set to select any number of read channels less than 4,016, in any pattern, providing the flexibility to select a specific area in the MEA and to increase the frame update rate based on the number of selected read channels.

F. Read Channel Array and MEA Variations

The gain and baseline offset variations across the 16,064 read channels are expected due to combinations of random

1932-4545 (c) 2019 IEEE. Personal use is permitted, but republication/redistribution requires IEEE permission. See http://www.ieee.org/publications_standards/publications/rights/index.html for more information.

This article has been accepted for publication in a future issue of this journal, but has not been fully edited. Content may change prior to final publication. Citation information: DOI 10.1109/TBCAS.2019.2953579, IEEE Transactions on Biomedical Circuits and Systems

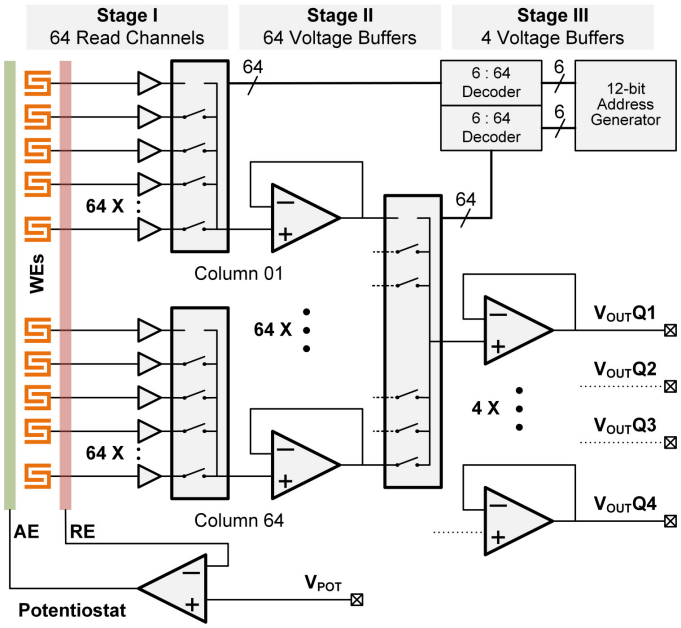

Fig. 6. Schematic diagram of the read channel array and stages of analog signal multiplexing driven by a 12-bit address generator and decoded for a fully customizable two-dimensional pattern.

variations related to the circuit topology, CMOS fabrication, and the transducer. These variations include TIA feedback resistance variation (R_{EQ}-σ), input offset of OP_{TJ} and OP_{TIA} ($V_{OS\text{-}TJ}$ and $V_{OS\text{-}TIA}$), WE geometry or surface area variation, and the WE surface condition. The interconnect parasitic resistance (R_{RT}) was approximated and simulated to vary from 0.5 kΩ to 1.8kΩ due to various distances from the read channel to its WE, which causes the potential at the WE to shift from V_{CM} based on the value of I_{IN}. However, an extreme case scenario of I_{IN} = 100nA and R_{RT} = 1.8kΩ yields a potential shift of 0.18mV, a negligible value in an electrochemical process. In summary, in an agreement to Eq. (2), the I_{IN} conversion gain variation is defined by the R_{EQ} with the addition of variations in WE geometry and surface condition. Meanwhile, the baseline variation is defined by the product of (1+ R_3/R_2) and V_{TJ} and V_{CM}, which is directly affected by the input offsets of OP_{TJ} and OP_{TIA}, respectively.

The R_{EQ}-σ variation is 0.11MΩ-σ in simulation and 0.48MΩ-σ in measurement across the 128 calibration channels. To capture the overall gain variation, chemical calibration experiments were performed to incorporate the effect of WE geometry and surface condition variations. The overall gain variation was measured to be 4.27MΩ-σ. The results suggest that the gain variation is dominated by the WE variations as the transducer. Therefore, chemical calibration should be performed periodically to account for the WE surface degradation or fouling. Due to the (1+ R_3/R_2) amplification to the 3.34mV-σ opamp input offset, the measured baseline variation is V_{OUT}-σ = 118mV or equal to the input-referred variation of I_{IN}-σ = 5.94nA. Gain and baseline offset variations were measured at the TIA V_{OUT} and defined as coefficients for each 16,064 read channel. With regulated temperature and power supply voltage, these values are mainly static and can be individually measured, stored, and used to calibrate each pixel during the data post-processing. The chemical calibration and sensitivity response experiment results are presented in Section VII-A.

IV. Supporting Modules and Circuit Boards

A. Power Supply Unit (PSU)

The biosensor system was built based on a dual-rail power supply to provide both positive and negative side of signal readings with a reference to common ground (0V). The PSU supplies two dual-rails at ±2.8V for supplying on-board controllable voltage regulator that supplies the CMOS MEA microchip and at ±3.3V for supporting other peripheral circuits. The PSU converts a 110V 60Hz AC to a single 12V DC, then converts the single 12V DC to dual-rail voltages using high-efficiency DC/DC buck and inverting buck-boost switching converters for positive and negative power lines, respectively. The PSU utilizes four integrated DC/DC switching power modules LMZM33602 (Texas Instruments, Dallas, USA) that can be configured as a standard step-down DC/DC converter or as an inverting DC/DC converter. As shown in Fig. 7(a) and (d), the PSU assembly contains AC entry module with fuse and passive filter, AC/DC voltage converter with 12V constant output, and four DC/DC switching power modules.

B. Sensor Circuit Board (S-PCB)

The custom CMOS MEA microchip described in Section III is housed in a 280 pin-grid array (PGA) package. The package sits on a zero-insertion-force socket which offers convenience for swapping CMOS MEA microchips in and out of the system. As shown in Fig. 7(b) and (f), the socket is centered in the S-PCB and surrounded by the support circuits for the CMOS MEA microchip. The top side holds two power regulating opamp to provide positive and negative potential (±1.5V to ±2.5V) for powering the CMOS MEA microchip. Their potential can be set dynamically by a digital potentiometer where its value is determined by a digital signal sent from the C-PCB. The bottom side holds switches for enabling on-chip circuits, voltage references, constant voltage regulator (±2.75V) for peripheral circuits, and connectors for temperature and pH sensor. The pH sensing circuit employs the instrumentation amplifier INA333 (Texas Instruments, Dallas, USA), which is in the same form of a previously discussed work [48].

C. Control Circuit Board (C-PCB)

As shown in Fig. 7(c) and depicted in a schematic in Fig. 1, the MCU chip Atmel SAM3X8E (Microchip, Chandler, USA) generates digital addresses for read channel selection, sets the potentiostat voltage, records PCBs and the CMOS biosensor microchip temperature, and monitors current and voltages. All information is processed and sent via a USB controller to the host computer. Pulse width modulator (PWM) generates accurate digital clocks to drive 12-bit digital counters. The digital-to-analog converter (DAC) generates specified waveforms for driving the on-chip potentiostat. The analog-to-digital converter (ADC) receives multiplexed signals from various monitoring readings, such as the power supply voltages, current flows in the power lines, and voltage potentials of AE and RE. The I^2C serial line provides communication to the digital potentiometer for CMOS MEA microchip voltage supply adjustment and communication to the temperature chip

1932-4545 (c) 2019 IEEE. Personal use is permitted, but republication/redistribution requires IEEE permission. See http://www.ieee.org/publications_standards/publications/rights/index.html for more information.

This article has been accepted for publication in a future issue of this journal, but has not been fully edited. Content may change prior to final publication. Citation information: DOI 10.1109/TBCAS.2019.2953579, IEEE Transactions on Biomedical Circuits and Systems

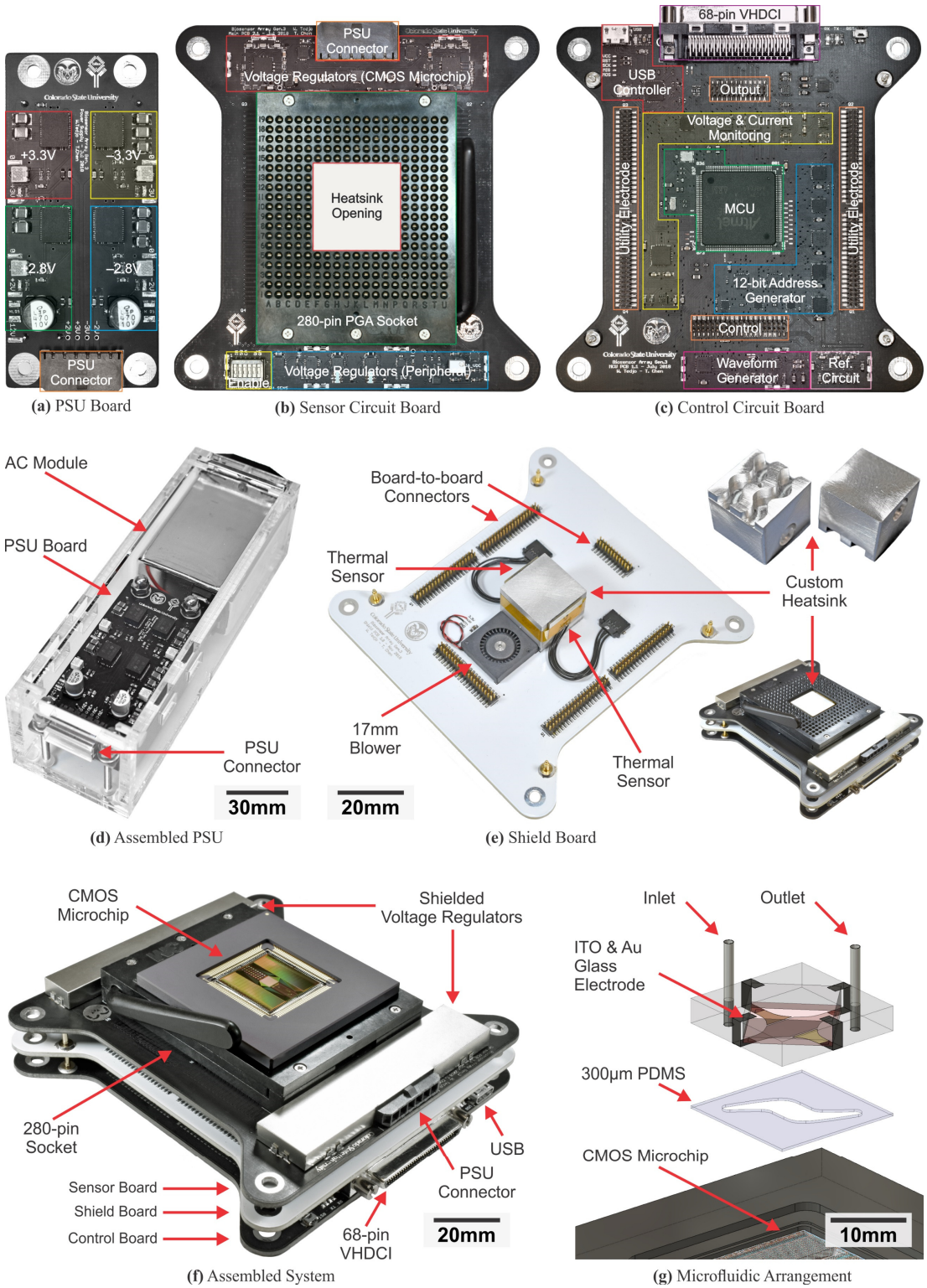

(a) PSU Board **(b)** Sensor Circuit Board **(c)** Control Circuit Board

(d) Assembled PSU **(e)** Shield Board

(f) Assembled System **(g)** Microfluidic Arrangement

Fig. 7. Custom designed and assembled printed circuit board. (a) Power supply unit circuit board with four DC/DC regulators. (b) Sensor circuit board holds the CMOS MEA microchip and the low noise voltage regulator. (c) Control circuit board with the MCU and other peripheral circuits. (d) Assembled Power supply unit. (e) Shield board with the custom heatsink and mini blower. (f) Assembled system with shielded analog components and installed the CMOS MEA microchip. (g) 3-D model of the microfluidic system with 300µm thick PDMS channel and integrated ITO and Au electrodes to a PMMA cover for pH sensing.

sensors. These control functions can be modified, and their responses can be monitored in real-time by users in the GUI. All analog output signals from the CMOS MEA microchip, pH sensor reading, and potentiostat are routed to the external DAQ for accurate analog acquisition through a 68-pin Very-High-Density Cable Interconnect (VHDCI) connector.

D. Shield Circuit Board (Sh-PCB)

The Sh-PCB is equipped with a custom milled heatsink and a 17mm mini blower fan as shown in Fig. 7(e). The heatsink

1932-4545 (c) 2019 IEEE. Personal use is permitted, but republication/redistribution requires IEEE permission. See http://www.ieee.org/publications_standards/publications/rights/index.html for more information.

This article has been accepted for publication in a future issue of this journal, but has not been fully edited. Content may change prior to final publication. Citation information: DOI 10.1109/TBCAS.2019.2953579, IEEE Transactions on Biomedical Circuits and Systems

creates a direct thermal contact (layered with thermally conductive pad/paste) with the bottom side of the CMOS MEA microchip ceramic package. Sh-PCB holds I^2C serial connections for two precision temperature sensors located on the heatsink. The temperature reading can be used to establish feedback control to the CMOS MEA microchip supply voltage to achieve desired power dissipation and specific temperatures at the MEA surface. The feedback is controlled by the MCU and its target temperature is set up by the user through the GUI. To ensure absolute thermal accuracy at the MEA surface, the thermal sensor readings were calibrated based on direct measurements at the MEA surface using a high accuracy (±0.05°C) thermometer, Traceable (Fisher Scientific, Hampton, USA).

E. Circuit Boards Assembly

The signal connections betweeen S-PCB, C-PCB, and Sh-PCB are made through half-pitch (1.27mm/0.05") headers at four corners of the board, with 160 side connectors dedicated for the 80 pairs of UEs. The top side connector is for analog output voltages, and the bottom side is for digital control signals as shown in Fig. 7(e) and (f). Sensitive electrical components (i.e. power supply regulators and voltage reference circuits) on both S-PCB and C-PCB were shielded to reduce EMI and to minimize accidental damage during wet chemical experiments. As depicted in Fig. 7(f), the stacking configuration forms rigid electrical and mechanical connections and allows direct vertical add-ons of other custom PCB for additional future expansions.

V. System-Level Integration

A. Microfluidic Platform

The microfluidic channel was made with stacks of 300µm Polydimethylsiloxane (PDMS) membrane as the fluidic channel and 3.0mm Poly(methyl-methacrylate) (PMMA) as a cover equipped with inlets and outlets. The PDMS membrane was molded and laser-cut to form a channel with various configurations, such as a single inlet with a single outlet or multiple inlets with one outlet, for different patterns of flow injection experiments. During a chemical imaging experiment, the PDMS-PMMA stack is attached to the CMOS MEA microchip with adequate pressure to form a sealed fluidic channel with 300µm height over the entire area of the MEA. The channel height can be adjusted by changing the PDMS membrane thickness to accommodate various fluidic volume.

Another version of the microfluidic channel employs a 10mm×10mm glass electrode integrated within the PMMA cover as shown in Fig. 7(g). Similar to previous work [6], the glass electrode with indium tin oxide (ITO) and Au pattern was fabricated using steps of photolithography and metal deposition process. This glass electrode can be multiplexed as a pH sensor or as alternative electrodes to the on-chip AE and RE. For further information, see Sections 2 and 3 of Supplementary Materials depicting the microfluidic setup used in experiments.

B. Data Acquisition and Real-time Visualization

The data interface between the electrochemical imaging system and the host computer is through the DAQ as illustrated in Fig 1. Each analog output signal from four quadrants is effectively sampled at a rate of 100kS/s by the DAQ. Each read channel is given 64µs window for its output signal to settle, resulting in approximately six sample points for each read channel before the control logic in the imaging system selects the next read channel. Once the output signals from all the read channels are sampled, the dataset is transferred to the host computer and stored. Promptly, a trigger command for starting the next frame acquisition occurs, in parallel with the start of data processing of the acquired frame. During data processing, the acquired data samples from each read channel are averaged over the six samples and stored as a single value representing a pixel in a 16-thousand pixel heatmap in real-time. Throughout the experiments, the DAQ was operated at the maximum effective 15.625kHz scanning rate per read channel. With all 4,016 read channels available in each quadrant, the frame update rate is approximately four FPS. A detailed flowchart of the real-time acquisition, processing, and visualization is illustrated in Section 5 in Supplementary Materials.

C. Graphic User Interface (GUI) Functionalities

A custom GUI was created on a host computer using MATLAB with a direct serial interface for communication with the C-PCB. The GUI provides comprehensive control and monitoring over ongoing events and environments of the system. There are two types of analytical chemistry methods supported by the system's GUI: amperometry and CV. In the amperometry mode, user can set the activation voltage, the number of frames to acquire, and the frame update rate up to four FPS. Electrochemical gradient measurement frames are recorded and shown in real-time as a 16-thousand pixel heatmap. In the voltammetry mode, user can set minimum and maximum potentiostat voltage, scan period, scan rate, and the number of cycles. Voltammetry results were recorded from 64 selected and uniformly distributed WEs across the MEA. Section 4 of Supplementary Materials shows a detailed list of GUI functions and real-time screenshots of the GUI.

VI. Experiment Setup and Materials

A. System Setup and Environmental Condition

The overall system, especially the CMOS MEA microchip, underwent a stringent initial verification phase to determine its electrical functionalities, sensitivity, selectivity, and spatiotemporal performance. Experiment results discussed in Section VII were performed at a constant power supply potential of ±1.65V to keep the CMOS MEA microchip temperature constant within 37±0.5°C. The on-chip potentiostat and three-electrode system were used to perform both amperometry and CV to generate the analytical chemistry results. The surface MEA is unmodified bare Pt electrodes. All experiments were performed at 5,003 feet (1,525m) altitude.

B. Materials

DI-H_2O at 18.2 MΩ.cm (Millipore Sigma, Burlington, USA) and ((±)-norepinephrine (+)-bitartrate salt (Sigma-Aldrich, St. Louis, USA) dissolved in DI-H_2O were used as the blank and neurotransmitter sample, respectively. Selectivity experiments used dissolved uric acid (UA) (Sigma-Aldrich, St. Louis, USA) as the secondary target analytes. For the oxygen experiments, DI-H_2O was degassed with a vacuum chamber and followed by nitrogen sparging to reach 5% of the atmospheric ambient

1932-4545 (c) 2019 IEEE. Personal use is permitted, but republication/redistribution requires IEEE permission. See http://www.ieee.org/publications_standards/publications/rights/index.html for more information.

This article has been accepted for publication in a future issue of this journal, but has not been fully edited. Content may change prior to final publication. Citation information: DOI 10.1109/TBCAS.2019.2953579, IEEE Transactions on Biomedical Circuits and Systems

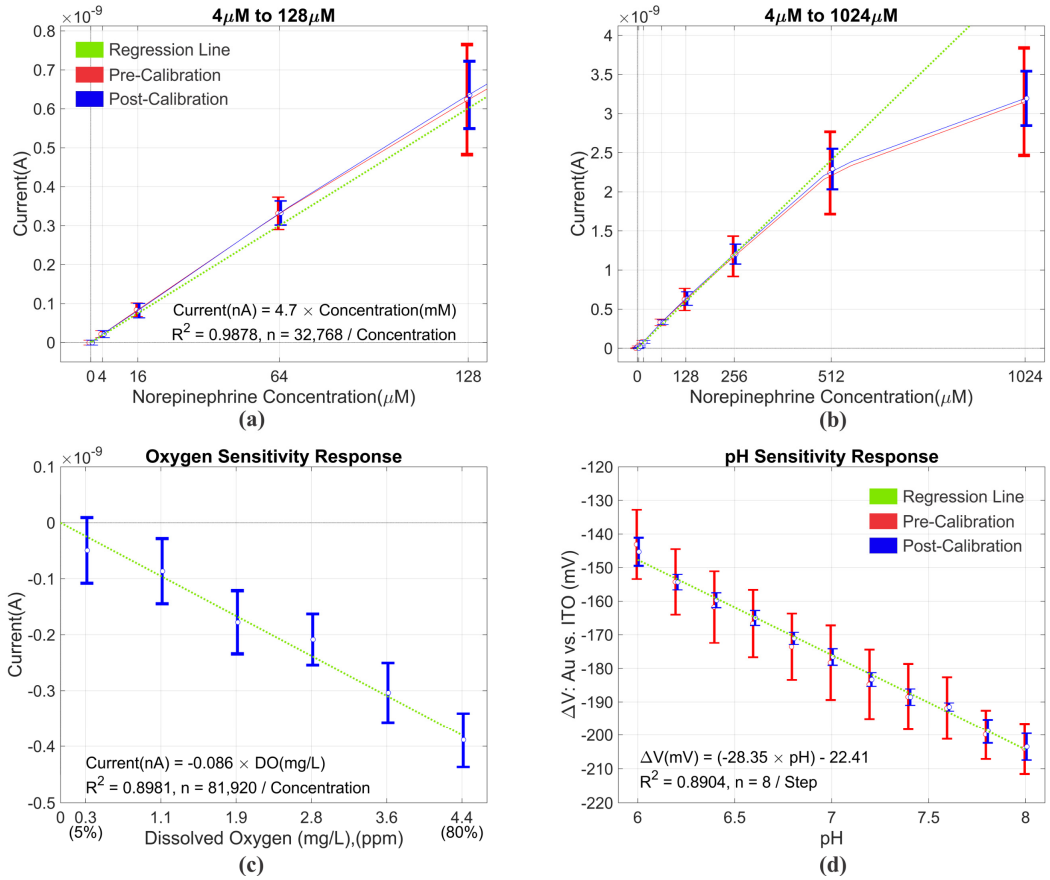

Fig. 8. (a) Sensitivity response generated from the step-response experiments, showing calibration curve and dynamic range of the system for NE concentration from 4μM to 128 μM, and (b) 4μM to 1,024 μM with n = 32,768 for each concentration. (c) Response to dissolved oxygen concentration with n = 81,920 per concentration. (d) Response to pH between 6.0 and 8.0 using the ITO and Au glass electrode. Error bars signify 1-σ value.

oxygen concentration. A commercial oxygen meter Oakton DO6+ (Cole-Parmer, Vernon Hills, USA) was used to confirm Dissolved Oxygen (DO) concentration before each sensing experiment. For pH calibration, different ratio mixtures of Sodium Phosphate Monobasic Monohydrate, H_4NaO_5P (Fisher Scientific, Hampton, USA), and Sodium Phosphate Dibasic Anhydrous, HNa_2O_4P (Fisher Scientific, Hampton, USA), a phosphate-buffer solution, were used to achieve 0.2pH resolution steps ranging from 6.0 pH to 8.0pH. The pH readings were verified using Fisherbrand™ Accumet™ AB15 (Fisher Scientific, Hampton, USA).

VII. Chemical Experiment Results

A. Amperometry and Sensitivity to Target Analytes

A flow injection system with two syringe pumps was set up for determining sensitivity to NE and DO concentrations. The flow injection setup allows sudden flow change between the control and sample to produce ranges of step-responses for different analyte concentrations. The differential values between control (DI-H^2O) and sample (concentrations of NE or DO) were recorded, processed, and used as the results.

An activation voltage of +0.6V was used in the amperometric sensing of NE. Fig. 8(a) and (b) summarizes dynamic range and sensitivity at the micromolar concentration range. This was used to establish the range of detection and to show the system's limitation in differentiating low concentrations of analytes down to 4μM and the linear dynamic range is limited below 512μM. This limitation may be influenced by several factors that limit the redox current flow between AE and WEs (e.g. the low ratio of AE to WE surface area, and limited voltage compliance and current driving strength of the on-chip potentiostat). Improvements to the dynamic range could be made by substituting the on-chip potentiostat with the external on-board potentiostat with a higher output compliance voltage and utilizing the ITO glass electrode to increase AE to WE area ratio. The sensitivity result shows a higher current response of 4.7pA/μM in comparison to the previous generation MEA of 3.35nA/mM [29], confirming that greater WE surface area increases steady-state current as discussed in Section III-C.

Fig. 8(c) depicts the system response to DO concentrations between 5% and 80% of the ambient oxygen concentration. Similar experiment method to sense NE was used with the activation voltage set to -0.7V to ensure complete oxygen reduction as previously described in [5], [37]. The system sensitivity for DO is 86pA/mg/L.

To fully appreciate the sensitivity limit of the system, calculations of blank (LoB), detection (LoD), and quantitation (LoQ), were also performed based on the Clinical and Laboratory Standards Institute (CLSI) EP17 guidelines [49]. Based on the NE chemical experiment, the LoD is calculated to be 41.0pA, an improvement over the previous system (52.5pA) [29], [41]. This indicates that the system can reproduce chemical images at similar or better fidelity. Refer to Section 6 of Supplementary Materials for more details on LoD.

1932-4545 (c) 2019 IEEE. Personal use is permitted, but republication/redistribution requires IEEE permission. See http://www.ieee.org/publications_standards/publications/rights/index.html for more information.

This article has been accepted for publication in a future issue of this journal, but has not been fully edited. Content may change prior to final publication. Citation information: DOI 10.1109/TBCAS.2019.2953579, IEEE Transactions on Biomedical Circuits and Systems

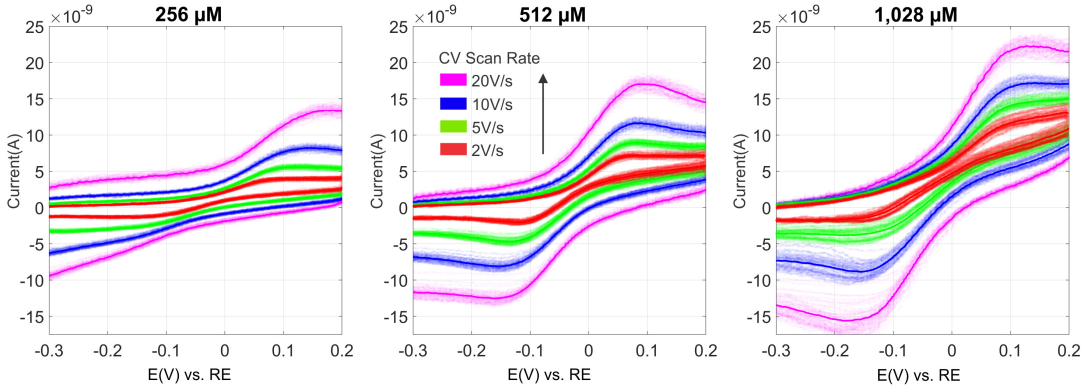

(a) Cyclic Voltammetry of Norepinephrine

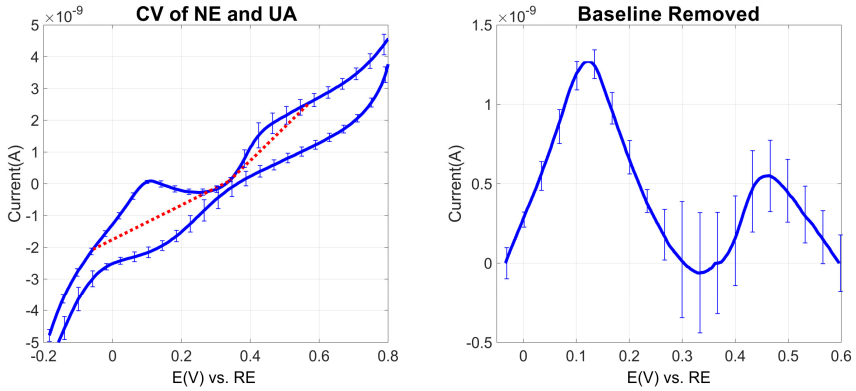

(b) Simultaneous Detection of Norepinehrine and Uric Acid

Fig. 9. Cyclic voltammetry analysis (a) CV response of various sweeping rate (2V/s to 20V/s) for three NE concentrations, 256µM, 512µM, and 1,028µM across 64 selected WEs. (b) Simultaneous detection of multiple analytes, a mixture of samples containing 0.5mM NE and 0.5mM UA across 64 selected WEs. Each error bar indicates 1-σ values.

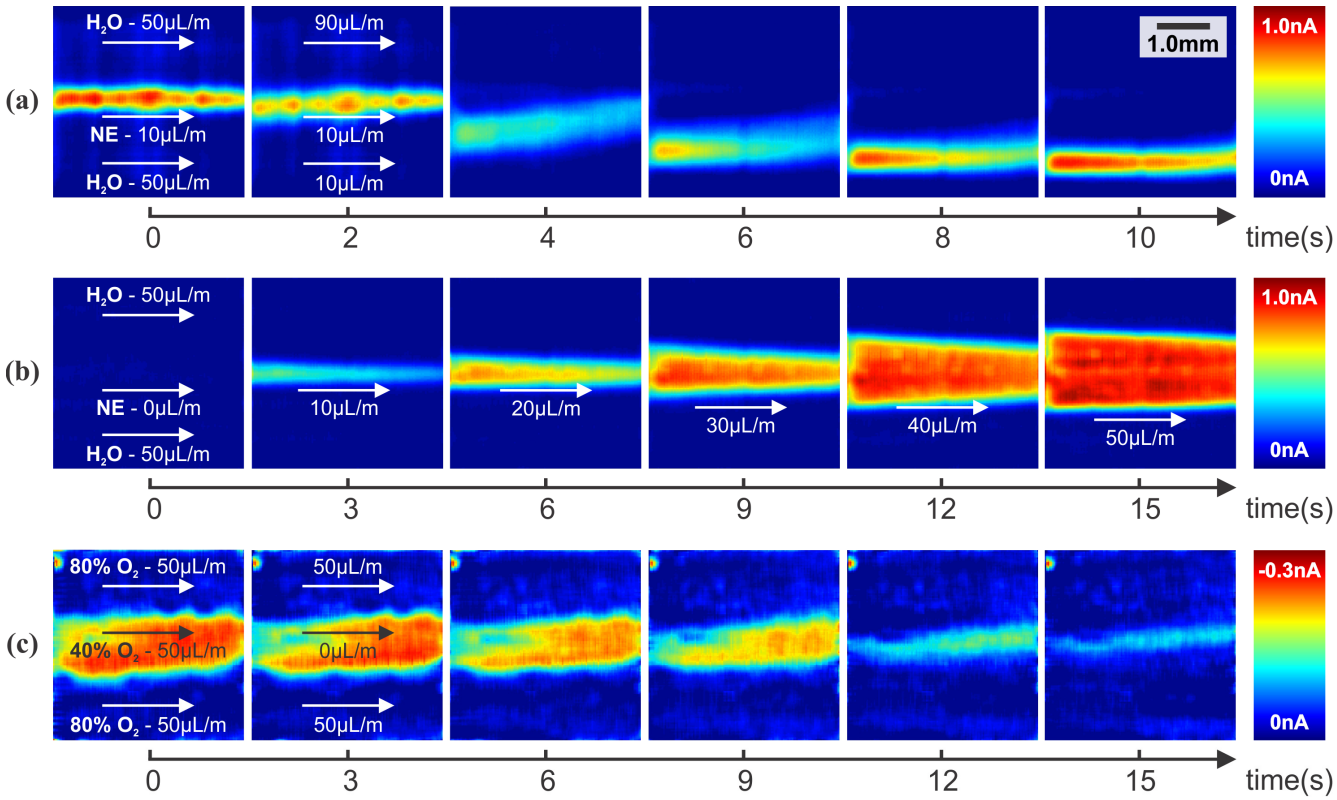

Fig. 10. Spatiotemporal resolution imaging results of flow injection. (a) and (b) Different pattern of flow injection of 100µM Norepinephrine. (c) Flow injection of DI-H^2O at different oxygen concentrations of 80% and 40%.

1932-4545 (c) 2019 IEEE. Personal use is permitted, but republication/redistribution requires IEEE permission. See http://www.ieee.org/publications_standards/publications/rights/index.html for more information.

This article has been accepted for publication in a future issue of this journal, but has not been fully edited. Content may change prior to final publication. Citation information: DOI 10.1109/TBCAS.2019.2953579, IEEE Transactions on Biomedical Circuits and Systems

B. pH Sensing

Due to the potential fluctuation of pH during electrochemical experiments, it is imperative to monitor pH in real-time to ensure predictability of the bio-sample behavior [50], [51]. Using the glass electrode described in Section V-A, the ITO and Au electrodes offer linear pH response of -28.35mV/pH for a range of 6.0pH to 8.0pH as shown in Fig. 8(d).

C. Cyclic Voltammetry and Simultaneous Detection of Different Target Analytes

Simultaneous detection of multiple target analytes has increasingly received more attention in biosensing. Recent works showed simultaneous detection of multiple analytes with Differential Pulse Voltammetry (DPV) [52]–[54]. Fig. 9(a) shows CV responses of NE at different concentrations with different scan rates. Each curve represents simultaneous recording from 64 (16 per quadrant) WEs uniformly distributed across the entire MEA area. Each read channel output is presented in opaque lines and their average is plotted as a solid line. The results are consistent with other reported results [55], [56] that showed the trend of increasing current peaks with higher analyte concentrations and the effect of scan rate [46]. Fig. 9(b) shows the CV results of 64 selected WEs for a 0.5mM NE and 0.5mM UA solution at 2V/s scan rate. The simultaneous detection result is indicated by the first current peak at 0.12V for NE and second current peak at 0.47V for UA.

D. Chemical Imaging

In ex vivo experiments with live samples, it is highly desirable to capture releases of target analytes in a high spatiotemporal resolution. As depicted in Fig. 10, screenshots of the electrochemical imaging heatmaps were generated from flow injection experiments. The experiments were performed with the support of three-inlet microfluidic channel (see Section 2 of Supplementary Materials) where two outer inlets were connected to two syringes containing control (DI-H_2O), set at initial flow rate of 50µL/min, and the middle inlet was connected to a syringe containing samples (i.e. NE and degassed 40%-oxygen DI-H_2O). The heatmap results were post-processed with DC offset adjustment, gain calibration, frame-to-frame smoothing, and simple spatial mean filtering [57] to show the gradient actions. However, excessive spatial mean filtering would decrease the spatial resolution below the initial 27.5µm pitch. For results presented in Fig. 10, the three-pixel spatial mean filtering was used.

The first imaging was performed by flowing 100µM NE at a 10µL/m between two streams of 50µL/m DI-H_2O. At t = 2s, an abrupt change of outer DI-H_2O flow rate to 90µL/m and 10µL/m was introduced to shifts of the constant NE flow to the bottom corner. The imaging results are shown in Fig. 10(a). The second imaging experiment was performed by introducing rapid increase of NE flow rate from 0µL/m to 50µL/m within 15s, creating a wider NE flow pattern in the middle with the increase in NE flow rate. The results are shown in Fig. 10(b).

TABLE II
SYSTEM-LEVEL GENERAL SPECIFICATIONS

Parameters	Condition	Min	Max	Unit
Read Channel Input Current	V_{DD} = ±1.65V	-74.0	72.3	nA
Read Channel Switch Rate	V_{DD} = ±1.65V		1.0	MHz
Potentiostat Compliance	V_{DD} = ±1.65V	-1.59	1.62	V
Potentiostat Scan Rate	V_{DD} = ±1.65V		5.0	kV/s
Power Supply Voltage	CMOS microchip V_{DD}	±1.5	±2.5	V
MEA Surface Temp.	V_{DD} = ±1.5 to ±2.0V	26.7	63.1	℃
MEA Surface Temp.	V_{DD} = ±1.65V @ 24℃	37.1	38.2	℃
Power Dissipation (V_{DD} = ±1.65V)	CMOS microchip		957	µW
	Entire system		1,242	µW
DAQ Sampling Rate	Each quadrant		100	kS/s
DAQ LSB	12-bit resolution	12.2	61.0	pA
Imaging Frame Rate	Amperometry		4	FPS
Norepinephrine Response	4µM to 512µM	4.7		pA/µM
Dissolved Oxygen Response	0.3mg/L to 4.4mg/L	86		pA/mg/L
pH Response	6.0pH to 8.0pH	-28.3		mV/pH
Limit of Blank		10.6		pA
Limit of Detection		41.0		pA

TABLE III
STATE-OF-THE-ART ELECTROCHEMICAL BIOSENSOR WITH MICROELECTRODE ARRAY

Parameters	CMOS		Working Electrode					Read Channel				Imaging Performance			On-Chip	
	Tech	Die Size	Sense Area	Count	Material	Size	Pitch	Count	BW	Input Noise	Power per Ch.	Imaging Result	Frame Rate	Conc. (Analyte)	Pot.	RE/ AE
Ref.	µm	mm	mm	-	-	µm	µm	-	kHz	pA_{RMS}	µW	-	FPS	Molar	-	-
[21]	0.18	12×8.9	4.5×2.4	59,760	Pt Black	3×7.5	13.5	28	10	120	178	No	-	200µ (DA)	No	No
[24]	0.5	-	1.2×1.2	1,024	Au	7×7	37	1	-	-	73.5	No	-	0.1 (KFe)	Yes	No
[25]	0.5	3×3	0.4×0.2	100	Ti/Pt	15×15	40×20	100	0.1	0.15	-	Yes	200	0.35µ (DA)	Yes	No
[26]	0.18	10.4×10.4	5.0×5.0	400	Au/Pt/Ti	40	250	400	-	1	1.57	Yes	8	10 (H_2O_2)	Yes	No
[27]	0.6	7.5×7.5	0.6×0.6	256	Au/Cr	10×10	35	1	-	3	430	Yes	1.4	0.1 (KFe)	No	Yes
[28]	0.35	7.5×4.8	3.2×3.2	1,024	Pt Black	25	100	32	1	58.5	-	Yes	90	30m(H_2O_2)	Yes	Yes
[29]	0.6	19×19	2.0×2.0	8,192	Pt	17.5×15	25×30	64	10	52	1,875	Yes	0.03	8µ (NE)	Yes	Yes
[30]	0.35	5×5	1.0×1.0	1,024	Au	15×15	30	1,024	4.4	0.47	12.2	Yes	10,000	10m (DA)	No	No
[31]	0.35	3.8×3.8	1.8×1.8	256	Au	20×20	114	16	150	1,040	2,681	Yes	-	100µ (Fe)	Yes	Yes
[32]	0.18	3×1.4	1.2×0.8	50	Al	60×60	160×120	50	-	4,680	4,900	No	2	-	No	Yes
[33]	0.18	5×5	3.2×3.2	4,096	Au	45×45	50	4,096	26	0.6	23	No	-	125n (FF)	No	No
[34]	0.35	3.8×3.1	3.2×2.4	192	Au	100	200	96	1	24	188	No	-	2m (DA)	Yes	Yes
This work[a]	0.6	19×19	3.6×3.6	16,064	Pt	17.5×17.5	27.5	16,064	5.66	42.8	59.6	Yes	4	4µ (NE)	Yes	Yes
This work[b]				4,016				4,016	3.56	59.7	39.6					

[a] Vsupply = ±1.65V, Surface Temp. ≈ 37.5℃ at 24℃ ambient. Four active quadrants. Optimal temperature for ex vivo experiments.
[b] Vsupply = ±1.50V, Surface Temp. ≈ 25.3℃ at 24℃ ambient. One active quadrant. Minimum supply potential with no significant performance reduction.
Analytes: DA: dopamine, KFe: Potassium ferricyanide (K3Fe(CN)6), NE: Norepinephrine, Fe: ferrocene (Fe(C5H5)2), FF: Ferro/Ferricyanide.

1932-4545 (c) 2019 IEEE. Personal use is permitted, but republication/redistribution requires IEEE permission. See http://www.ieee.org/publications_standards/publications/rights/index.html for more information.

This article has been accepted for publication in a future issue of this journal, but has not been fully edited. Content may change prior to final publication. Citation information: DOI 10.1109/TBCAS.2019.2953579, IEEE Transactions on Biomedical Circuits and Systems

Finally, as presented in Fig. 10(c), the imaging for DO concentration was started with 50μL/m flow rates of the 80% and 40% DO. A sudden stop of the 40% DO concentration was introduced at t = 2s and followed by the middle flow signal decaying within 10s. The resulting heatmaps with hundreds of pA gradients not only show sensitivity performance but also demonstrate the spatiotemporal resolution of the system.

VIII. Discussions and Conclusions

A high spatiotemporal resolution electrochemical biosensor system with CMOS microchip employing a novel Pt MEA is presented. Flow injection electrochemical experiments confirmed that the highly integrated electrochemical imaging system provided excellent spatial and temporal resolutions for most biological electrochemical sensing experiments. Table I lists the detailed performance specifications achieved at the circuit level. Table II lists the general system-level specifications of the imaging system.

Comparing to other recent work in experimental MEA systems, the highly integrated electrochemical imaging system fares well in many categories. Table III provides a summary of the key features of the imaging system in comparison with other existing MEA systems performing electrochemical sensing. Desirable features from a chemical imaging device are high pixel counts, high spatial and temporal resolution, high sensitivity to target analytes, integration of the electronics and electrodes, and integration of other supporting systems (e.g. temperature control, pH sensor, bio-sample handlings). An existing work with the highest spatial resolution was presented by Dragas [21] focused on the electrophysiology performance and shows minimal electrochemical sensing performance with no chemical imaging results. Another work with the highest temporal resolution presented by White [30] successfully performed imaging of neurotransmitter, however, with high a concentration of 10mM Dopamine (DA) and on a 1,024-pixel array. Their results show 0.5nA current response to 10mM DA, while our system shows similar current response for 0.1mM NE. DA and NE are in the same neurotransmitter family with identical electrochemical process of two electrons oxidation; thus, our WE geometry configuration has approximately 100× sensitivity to the target analyte in comparison to the results in [30]. This paper presents a system with the highest number of pixels that provides the most comprehensive chemical experiments and verifies the chemical imaging results using multiple target analytes (i.e. NE, UA, and DO) at micromolar concentrations. Furthermore, our system also provides real-time pH monitoring, real-time temperature control, and an improved microfluidic system based on the previous system used in ex vivo experiments [29].

The system presented in this paper offers all-around chemical imaging capability prepared for performing biological-significant studies. Applications of such system include the expansion of existing works in single-cell viability in Assisted Reproduction Technology (ART) [3], [58], rapid cytometry [59], [60], and cellular physiology related to degenerative diseases and cancer developments [61], [62].

As the system core, the versatility of the CMOS MEA microchip allows extensive feature expansions and improvements at the board and system-level. First, a custom data acquisition design, similar to previously reported work [28], [30], would allow the system to perform higher temporal resolution chemical imaging of all 16,064 read channels up to 244FPS from the existing 4FPS. Second, the 80 pairs of general-purpose UE are available for incorporating additional functionality such as localized electrical stimulations and impedance sensing. Finally, the bare Pt MEA provides opportunities for further improvement in sensitivity and selectivity with enhanced surface modifications, such as gas permeable coated electrodes for oxygen detection [1], [2], enzyme-based coating for glucose and lactate sensing [4]–[6], or polymer-based coating for improved simultaneous detection of various neurotransmitters [52]–[54].

Acknowledgements

The CMOS MEA microchip with Pt MEA was manufactured by Broadcom Inc. (San Jose, CA). The authors would like to thank Luke Schwerdtfeger and Dr. Stuart Tobet in the Department of Biomedical Sciences, Dr. Charles Henry in the Department of Chemistry, August DeMann in the Department of Physics, and Ming-Hao Cheng and Yusra Obeidat in the Department of Electrical & Computer Engineering at Colorado State University (Fort Collins, CO) for their useful discussions and assistances. This work was partially supported by two grants from the National Science Foundation (GDE-0841259 and GDE-1450032).

References

[1] J. Park, Y. K. Pak, and J. J. Pak, "A microfabricated reservoir-type oxygen sensor for measuring the real-time cellular oxygen consumption rate at various conditions," *Sensors Actuators, B Chem.*, vol. 147, no. 1, pp. 263–269, 2010.

[2] C. C. Wu, H. N. Luk, Y. T. T. Lin, and C. Y. Yuan, "A Clark-type oxygen chip for in situ estimation of the respiratory activity of adhering cells," *Talanta*, vol. 81, no. 1–2, pp. 228–234, 2010.

[3] K. Hiramoto *et al.*, "Development of Oxygen Consumption Analysis with an on-Chip Electrochemical Device and Simulation," *Anal. Chem.*, vol. 89, no. 19, pp. 10303–10310, 2017.

[4] A. F. Revzin, K. Sirkar, A. Simonian, and M. V. Pishko, "Glucose, lactate, and pyruvate biosensor arrays based on redox polymer/oxidoreductase nanocomposite thin-films deposited on photolithographically patterned gold microelectrodes," *Sensors Actuators, B Chem.*, vol. 81, no. 2–3, pp. 359–368, 2002.

[5] Y. Obeidat, A. J. Evans, W. Tedjo, A. J. Chicco, E. Carnevale, and T. W. Chen, "Monitoring oocyte/embryo respiration using electrochemical-based oxygen sensors," *Sensors Actuators, B Chem.*, vol. 276, no. February, pp. 72–81, 2018.

[6] Y. Obeidat *et al.*, "A Multi-Sensor System for Measuring Bovine Embryo Metabolism," *Biosens. Bioelectron.*, vol. 126, no. September, pp. 615–623, 2018.

[7] F. Bedioui and N. Villeneuve, "Electrochemical nitric oxide sensors for biological samples–Principle, selected examples and applications," *Electroanalysis*, vol. 15, no. 1, pp. 5–18, 2003.

[8] B. J. Privett, J. H. Shin, and M. H. Schoenfisch, "Electrochemical nitric oxide sensors for physiological measurements," *Chem. Soc. Rev.*, vol. 39, no. 6, p. 1925, 2010.

[9] H. M. Jafari, K. Abdelhalim, L. Soleymani, E. H. Sargent, S. O. Kelley, and R. Genov, "Nanostructured CMOS wireless ultra-wideband label-free PCR-free DNA analysis SoC," *IEEE J. Solid-State Circuits*, vol. 49, no. 5, pp. 1223–1241, 2014.

[10] D. Jambrec, K. Lammers, T. Bobrowski, S. Pöller, W. Schuhmann, and A. Ruff, "Amperometric Detection of dsDNA Using an Acridine-Orange-Modified Glucose Oxidase," *Chempluschem*, vol. 82, no. 11, pp. 1311–1314, 2017.

[11] E. S. Bucher and R. M. Wightman, "Electrochemical Analysis of Neurotransmitters.," *Annu. Rev. Anal. Chem. (Palo Alto. Calif).*, vol. 8, pp. 239–61, 2015.

1932-4545 (c) 2019 IEEE. Personal use is permitted, but republication/redistribution requires IEEE permission. See http://www.ieee.org/publications_standards/publications/rights/index.html for more information.

This article has been accepted for publication in a future issue of this journal, but has not been fully edited. Content may change prior to final publication. Citation information: DOI 10.1109/TBCAS.2019.2953579, IEEE Transactions on Biomedical Circuits and Systems

[12] B. Si and E. Song, "Recent Advances in the Detection of Neurotransmitters," *Chemosensors*, vol. 6, no. 1, p. 1, 2018.

[13] C. A. Thomas, P. A. Springer, G. E. Loeb, Y. Berwald-Netter, and L. M. Okun, "A miniature microelectrode array to monitor the bioelectric activity of cultured cells," *Exp. Cell Res.*, vol. 74, no. 1, pp. 61–66, Sep. 1972.

[14] A. Stett *et al.*, "Biological application of microelectrode arrays in drug discovery and basic research," *Anal. Bioanal. Chem.*, vol. 377, no. 3, pp. 486–495, 2003.

[15] M. Fejtl, A. Stett, W. Nisch, K. H. Boven, and A. Möller, "On micro-electrode array revival: Its development, sophistication of recording, and stimulation," *Adv. Netw. Electrophysiol. Using Multi-Electrode Arrays*, pp. 24–37, 2006.

[16] M. E. J. Obien, K. Deligkaris, T. Bullmann, D. J. Bakkum, and U. Frey, "Revealing neuronal function through microelectrode array recordings," *Front. Neurosci.*, vol. 9, no. JAN, p. 423, 2015.

[17] B. Eversmann *et al.*, "A 128 × 128 CMOS Biosensor Array for Extracellular Recording of Neural Activity," *IEEE J. Solid-State Circuits*, vol. 38, no. 12, pp. 2306–2317, 2003.

[18] D. Tsai, D. Sawyer, A. Bradd, R. Yuste, and K. L. Shepard, "A very large-scale microelectrode array for cellular-resolution electrophysiology," *Nat. Commun.*, vol. 8, no. 1, 2017.

[19] M. Ballini *et al.*, "A 1024-channel CMOS microelectrode array with 26,400 electrodes for recording and stimulation of electrogenic cells in vitro," *IEEE J. Solid-State Circuits*, vol. 49, no. 11, pp. 2705–2719, 2014.

[20] L. Berdondini *et al.*, "Active pixel sensor array for high spatio-temporal resolution electrophysiological recordings from single cell to large scale neuronal networks," *Lab Chip*, vol. 9, no. 18, pp. 2644–2651, 2009.

[21] J. Dragas *et al.*, "In Vitro Multi-Functional Microelectrode Array Featuring 59760 Electrodes, 2048 Electrophysiology Channels, Stimulation, Impedance Measurement, and Neurotransmitter Detection Channels," *IEEE J. Solid-State Circuits*, vol. 52, no. 6, pp. 1576–1590, 2017.

[22] T. Chi *et al.*, "A Multi-Modality CMOS Sensor Array for Cell-Based Assay and Drug Screening," *IEEE Trans. Biomed. Circuits Syst.*, vol. 9, no. 6, pp. 801–814, 2015.

[23] J. S. Park *et al.*, "1024-Pixel CMOS Multimodality Joint Cellular Sensor/Stimulator Array for Real-Time Holistic Cellular Characterization and Cell-Based Drug Screening," *IEEE Trans. Biomed. Circuits Syst.*, vol. 12, no. 1, pp. 80–94, 2018.

[24] S. Hwang, C. N. LaFratta, V. Agarwal, Xin Yu, D. R. Walt, and S. Sonkusale, "CMOS Microelectrode Array for Electrochemical Lab-on-a-Chip Applications," *IEEE Sens. J.*, vol. 9, no. 6, pp. 609–615, Jun. 2009.

[25] B. N. Kim, A. D. Herbst, S. J. Kim, B. A. Minch, and M. Lindau, "Parallel recording of neurotransmitters release from chromaffin cells using a 10x10 CMOS IC potentiostat array with on-chip working electrodes," *Biosens. Bioelectron.*, vol. 41, no. 1, pp. 736–744, 2013.

[26] K. Y. Inoue *et al.*, "LSI-based amperometric sensor for bio-imaging and multi-point biosensing," *Lab Chip*, vol. 12, no. 18, pp. 3481–3490, 2012.

[27] T. Kuno, K. Niitsu, and K. Nakazato, "Amperometric electrochemical sensor array for on-chip simultaneous imaging," *Jpn. J. Appl. Phys.*, vol. 53, no. 4 SPEC. ISSUE, pp. 1–7, 2014.

[28] J. Rothe, O. Frey, A. Stettler, Y. Chen, and A. Hierlemann, "Fully integrated CMOS microsystem for electrochemical measurements on 32 × 32 working electrodes at 90 frames per second," *Anal. Chem.*, vol. 86, no. 13, pp. 6425–6432, 2014.

[29] W. Tedjo *et al.*, "Electrochemical biosensor system using a CMOS microelectrode array provides high spatially and temporally resolved images," *Biosens. Bioelectron.*, vol. 114, pp. 78–88, Aug. 2018.

[30] K. A. White, G. Mulberry, and B. N. Kim, "Rapid 1024-pixel Electrochemical Imaging at 10,000 Frames per Second using Monolithic CMOS Sensor and Multifunctional Data Acquisition System," *IEEE Sens. J.*, vol. 18, no. 13, pp. 1–1, 2018.

[31] C. Giagkoulovits *et al.*, "A 16 x 16 CMOS Amperometric Microelectrode Array for Simultaneous Electrochemical Measurements," *IEEE Trans. Circuits Syst. I Regul. Pap.*, vol. 1, pp. 1–11, 2018.

[32] A. Hassibi and T. H. Lee, "A programmable 0.18-μm CMOS electrochemical sensor microarray for biomolecular detection," *IEEE Sens. J.*, vol. 6, no. 6, pp. 1380–1388, 2006.

[33] A. C. Sun, S. Member, E. Alvarez-fontecilla, A. G. Venkatesh, E. Aronoff-spencer, and D. A. Hall, "High-Density Redox Amplified Coulostatic Discharge-Based Biosensor Array," pp. 1–11, 2018.

[34] M. H. Nazari, H. Mazhab-Jafari, L. Leng, A. Guenther, and R. Genov, "CMOS neurotransmitter microarray: 96-channel integrated potentiostat with on-die microsensors," *IEEE Trans. Biomed. Circuits Syst.*, vol. 7, no. 3, pp. 338–348, 2013.

[35] K. Ino *et al.*, "Densified electrochemical sensors based on local redox cycling between vertically separated electrodes in substrate generation/chip collection and extended feedback modes," *Anal. Chem.*, vol. 86, no. 8, pp. 4016–4023, 2014.

[36] A. Kara *et al.*, "Electrochemical imaging for microfluidics: A full-system approach," *Lab Chip*, vol. 16, no. 6, pp. 1081–1087, 2016.

[37] N. Kasai, A. Shimada, T. Nyberg, and K. Torimitsu, "An electrochemical sensor array and its application to real-time brain slice imaging," *Electron. Commun. Japan*, vol. 92, no. 9, pp. 217–221, 2009.

[38] W. Pettine, M. Jibson, T. Chen, S. Tobet, P. Nikkel, and C. S. Henry, "Characterization of novel microelectrode geometries for detection of neurotransmitters," *IEEE Sens. J.*, vol. 12, no. 5, pp. 1187–1192, 2012.

[39] J. B. Wydallis *et al.*, "Spatiotemporal norepinephrine mapping using a high-density CMOS microelectrode array," *Lab Chip*, vol. 15, no. 20, pp. 4075–4082, 2015.

[40] R. M. Feeny, J. B. Wydallis, T. Chen, S. Tobet, M. M. Reynolds, and C. S. Henry, "Analysis of Nitric Oxide from Chemical Donors Using CMOS Platinum Microelectrodes," *Electroanalysis*, vol. 27, no. 5, pp. 1104–1109, 2015.

[41] W. Tedjo *et al.*, "Design of an integrated microelectrode array system for high spatiotemporal resolution chemical imaging," in *2016 IEEE Biomedical Circuits and Systems Conference (BioCAS)*, 2016, pp. 46–49.

[42] T. J. Davies *et al.*, "The linear sweep voltammetry of random arrays of microdisc electrodes: Fitting of experimental data," *J. Electroanal. Chem.*, vol. 592, no. 2, pp. 126–130, Jul. 2006.

[43] T. J. Davies and R. G. Compton, "The cyclic and linear sweep voltammetry of regular and random arrays of microdisc electrodes: Theory," *J. Electroanal. Chem.*, vol. 585, no. 1, pp. 63–82, 2005.

[44] L. Pilon and H. N. Wang, "Accurate Simulations of Electric Double Layer Capacitance of Ultramicroelectrodes," *J. Phys. Chem. C*, vol. 115, no. 33, pp. 16711–16719, 2011.

[45] D. P. Manica, Y. Mitsumori, and A. G. Ewing, "Characterization of electrode fouling and surface regeneration for a platinum electrode on an electrophoresis microchip," *Anal. Chem.*, vol. 75, no. 17, pp. 4572–4577, 2003.

[46] A. J. Bard and L. R. Faulkner, *Electrochemical Methods: Fundamentals and Applications*. 2000.

[47] J. Hasegawa, S. Uno, and K. Nakazato, "Amperometric electrochemical sensor array for On-chip simultaneous imaging: Circuit and microelectrode design considerations," *Jpn. J. Appl. Phys.*, vol. 50, no. 4 PART 2, pp. 1–9, 2011.

[48] L. Te Yin, J. C. Chou, W. Y. Chung, T. P. Sun, and S. K. Hsiung, "Separate structure extended gate H+-ion sensitive field effect transistor on a glass substrate," *Sensors Actuators, B Chem.*, vol. 71, no. 1–2, pp. 106–111, 2000.

[49] D. A. Armbruster and T. Pry, "Limit of blank, limit of detection and limit of quantitation," *Clin. Biochem. Rev.*, vol. 29, no. Suppl 1, pp. S49–S52, Aug. 2008.

[50] A. Salis and M. Monduzzi, "Not only pH. Specific buffer effects in biological systems," *Curr. Opin. Colloid Interface Sci.*, vol. 23, pp. 1–9, 2016.

[51] S. R. S. Bibby, D. A. Jones, R. M. Ripley, and J. P. G. Urban, "Metabolism of the Intervertebral Disc : Effects of Low Levels of Oxygen , Glucose , and pH on Rates of Energy Metabolism of Bovine Nucleus Pulposus Cells," vol. 30, no. 5, pp. 487–496, 2005.

[52] A. A. Ensafi, M. Taei, and T. Khayamian, "A differential pulse voltammetric method for simultaneous determination of ascorbic acid, dopamine, and uric acid using poly (3-(5-chloro-2-hydroxyphenylazo)-4,5-dihydroxynaphthalene-2,7-disulfonic acid) film modified glassy carbon electrode," *J. Electroanal. Chem.*, vol. 633, no. 1, pp. 212–220, 2009.

[53] H. Sun *et al.*, "Gold nanoparticle-decorated MoS2 nanosheets for simultaneous detection of ascorbic acid, dopamine and uric acid," *RSC Adv.*, vol. 4, no. 52, p. 27625, 2014.

[54] S. Ben Aoun, "Nanostructured carbon electrode modified with N-doped graphene quantum dots–chitosan nanocomposite: a sensitive electrochemical dopamine sensor," *R. Soc. Open Sci.*, vol. 4, no. 11, p. 171199, Nov. 2017.

[55] N. G. Mphuthi, A. S. Adekunle, and E. E. Ebenso, "Electrocatalytic oxidation of Epinephrine and Norepinephrine at metal oxide doped phthalocyanine / MWCNT composite sensor," *Nat. Publ. Gr.*, no. May, pp. 1–20, 2016.

[56] K. Pihel, T. J. Schroeder, and R. M. Wightman, "Rapid and Selective Cyclic Voltammetric Measurements of Epinephrine and Norepinephrine

1932-4545 (c) 2019 IEEE. Personal use is permitted, but republication/redistribution requires IEEE permission. See http://www.ieee.org/publications_standards/publications/rights/index.html for more information.

This article has been accepted for publication in a future issue of this journal, but has not been fully edited. Content may change prior to final publication. Citation information: DOI 10.1109/TBCAS.2019.2953579, IEEE Transactions on Biomedical Circuits and Systems

as a Method To Measure Secretion from Single Bovine Adrenal Medullary Cells," vol. 66, no. 24, pp. 4532–4537, 1994.
[57] E. R. Davies, "Chapter 3 - Basic Image Filtering Operations," E. R. B. T.-C. and M. V. (Fourth E. Davies, Ed. Boston: Academic Press, 2012, pp. 38–81.
[58] L. Scott, J. Berntsen, D. Davies, J. Gundersen, J. Hill, and N. Ramsing, "Human oocyte respiration-rate measurement - Potential to improve oocyte and embryo selection?," *Reprod. Biomed. Online*, vol. 17, no. 4, pp. 461–469, 2008.
[59] K. Niitsu, S. Ota, K. Gamo, H. Kondo, M. Hori, and K. Nakazato, "Development of Microelectrode Arrays Using Electroless Plating for CMOS-Based Direct Counting of Bacterial and HeLa Cells," *IEEE Trans. Biomed. Circuits Syst.*, vol. 9, no. 5, pp. 607–619, 2015.
[60] M. Xu, R. Wang, and Y. Li, "Electrochemical biosensors for rapid detection of Escherichia coli O157:H7," *Talanta*, vol. 162, no. August 2016, pp. 511–522, 2017.
[61] P. J. Ratcliffe, "Oxygen sensing and hypoxia signalling pathways in animals: The implications of physiology for cancer," *J. Physiol.*, vol. 591, no. 8, pp. 2027–2042, 2013.
[62] G. Solaini, A. Baracca, G. Lenaz, and G. Sgarbi, "Hypoxia and mitochondrial oxidative metabolism," *Biochim. Biophys. Acta - Bioenerg.*, vol. 1797, no. 6–7, pp. 1171–1177, 2010.

William Tedjo received the B.S. and Ph.D. in electrical engineering from Colorado State University, Fort Collins, CO in 2013 and 2019, respectively.

From 2013 to 2019, he actively involved in teaching assistantship and fellowship at the Department of Electrical and Computer Engineering (ECE), Colorado State University. In 2014, he worked for WhiteRidge Technologies, Fort Collins, CO, as a Circuit & Physical Design Engineer intern. Since 2019, he joined Sensata Technologies, Attleboro, MA, as a Senior Circuit Design Engineer.

His interests and research experiences include CMOS circuit design, board-level design and assembly, hardware-software interface, statistical analysis, data visualization, and system integration for electronic-based sensing devices.

Thomas Chen is a professor at the Department of Electrical and Computer Engineering (ECE) and School of Biomedical Engineering (SBME). He received his B.S. from Shanghai Jiaotong University and Ph.D. from the University of Edinburgh. He spent 4 years with Philips Semiconductors in Europe and 1 year with New Jersey Institute of Technology before joining Colorado State University. His research interests include all aspects of biosensors and bioelectronics and their applications to biology and biomedical sciences. Dr. Chen has over 150 refereed journal and conference publications in the areas of VLSI circuits and biosensor circuits and systems, and 4 US patents. Dr. Chen provided expert opinions for the Federal Trade Commission, and guest edited several IEEE and Elsevier journal issues on CMOS circuit designs and microelectronics. Dr. Chen is a senior member of IEEE and a member of the Steering Committee for IEEE Midwest Symposium on Circuits and Systems. He currently holds Business Challenge Endowment Professorship at Colorado State University.

1932-4545 (c) 2019 IEEE. Personal use is permitted, but republication/redistribution requires IEEE permission. See http://www.ieee.org/publications_standards/publications/rights/index.html for more information.